A novel strategy of thermal management system for battery energy storage system based on supercritical CO_2

Khan, Shahid Ali; Ahmad, Shakeel; Lau, Kwun Ting; Dong, Kejian; HE, Sihong; Liu, Huaqiang; Zhao, Jiyun

Published in:
Energy Conversion and Management

Published: 01/02/2023

Document Version:
Post-print, also known as Accepted Author Manuscript, Peer-reviewed or Author Final version

Published version (DOI):
10.1016/j.enconman.2023.116676

Publication details:
Khan, S. A., Ahmad, S., Lau, K. T., Dong, K., HE, S., Liu, H., & Zhao, J. (2023). A novel strategy of thermal management system for battery energy storage system based on supercritical CO_2. *Energy Conversion and Management*, *277*, Article 116676. https://doi.org/10.1016/j.enconman.2023.116676

A novel strategy of thermal management system for battery energy storage system based on supercritical CO_2 ⋆

Shahid Ali Khan[a], Shakeel Ahmad[b], Kwun Ting Lau[a], Kejian Dong[a], Sihong HE[a], Huaqiang Liu[c], Jiyun Zhao[a*]

[a]*Department of Mechanical Engineering, City University of Hong Kong, Hong Kong, China*
[b]*Department of Building Environment and Energy Engineering, The Hong Kong Polytechnic University*
[c]*Naval Architecture and Ocean Engineering College, Dalian Maritime University, Liaoning, China*

Abstract

Supercritical CO_2 (sCO_2) is examined as a working fluid for the first time in a unique thermal management strategy that aims to control undesirable thermal behavior in battery cooling applications. In the pseudocritical region, sCO_2 has a high volumetric thermal capacity with low critical pressure and temperature, which not only reduces system complexity and costs but also eliminates the possibility of two-phase critical heat flux and flow instabilities. A pack of 20×5 Li-ion batteries for battery energy storage system (BESS) applications was designed and employed in a structurally optimized thermal management system. Further, the effects of different dielectric fluid media on the number of flow inlets, flow rates, and discharge rates were numerically investigated. Compared with conventional coolants, sCO_2 exhibited superior temperature suppression and temperature differences. The rise in both mass flow rate and the number of flow inlets significantly suppressed the maximum temperature and temperature difference. Besides, the pressure drop was slightly increased with the increased mass flow rate. Moreover, sCO_2 controls the thermal behavior of a large battery pack at high discharge rates within an optimal range. The finding offers various attributes for cooling large battery packs, particularly for high-power grid stations and BESS. In the future, the practicality of high working pressures and power requirements for the pump should be carefully studied.

Keywords: Supercritical CO_2, Battery energy storage systems, Dielectric fluid, Thermal management system, Li-ion battery

2010 MSC: 00-01, 99-00

1. Introduction

Significant changes in human living standards have emerged as a result of the rapid rise of society and the economy. Nevertheless, increased energy consumption eventually leads to the depletion of fossil fuel resources and environmental contamination issues. Renewable energy sources have gained popularity in recent years, with research indicating an

⋆Fully documented templates are available in the elsarticle package on CTAN.

Email address: jiyuzhao@cityu.edu.hk (Jiyun Zhao[a*])

upward tendency in their advancement. This is due to the increased focus on environmental pollution brought by the use of traditional energies [1]. Furthermore, the explosive growth of factories, industries, and gasoline engine-based vehicles contributes to pollution. Carbon dioxide emissions cause global warming and the greenhouse effect, which reduce agricultural production and raise sea levels. [2]. Therefore, electric energy storage (EES) has a vital role in making the environment safe and friendly for humankind. EES is capable of storing the electricity or energy used to generate electricity and releasing it for use at a later time when its utilization is more advantageous. Redox fuel cells, flywheels, Sodium Ion Sulfur (NaS) batteries, valve-regulated lead acid batteries, Li-ion batteries, compressed air energy storage, magnetic superconducting energy storage, and pumped-storage systems are some examples of these technologies [3, 4, 5]. Some of the selected EES are listed in Table 1. Among them, Li-ion batteries are very popular in today's world because they are eco-friendly, have a high energy density, are lightweight and compact, have higher charge cycles, require little maintenance, and have a low self-discharge rate. Similar to any other technology, there are some limitations that must be weighed against the advantages. Li-ion batteries have a two- to three-year lifespan after production, are sensitive to extreme temperatures, cannot be recharged after fully discharging, and can burst into flames if the separator is damaged. Many researchers are working to overcome these issues [6, 7, 8]. The free-standing and foldable V_2O_3/multichannel carbon nanofiber (V_2O_3/MCCNF) composites were developed via electrospinning and subsequent carbonization by zhang et al [9]. The ultralong lifespan is obtained with a high capacity of 487.8 mAhg^{-1} even after 5000 cycles at a high current density of 5 Ag^{-1} and a degradation rate of only 0.00323$\%$, demonstrating the best performance among the reported V_2O_3-based anodes. With the growing adoration and reliance on Li-ion batteries for their power and convenience, their disposal has become a political and environmental concern. For instance, according to the International Energy Agency, electric vehicles produced in 2019 alone generated 500,000 tons of Li-ion battery waste, and by 2040, the overall amount of waste produced might reach as high as 8 million tons [10]. Numerous researchers have focused on different techniques for the Li-ion batteries' recycling [11, 12]. Roy et al.[10] discussed eco-friendly green recycling techniques for used Li-ion batteries, such as bioleaching, the waste-for-waste approach, and electrodeposition.

BESS are widely used in a variety of fields, including manufacturing, retail, transportation, residential, and grid-based power generation, due to their remarkable properties, such as high specific energy, a smooth discharge profile, a high energy density, a minimal storage effect, and a relatively low resistance. Currently, Li-ion batteries are the most

widely used form of grid-connected battery storage, making up more than 90% of the market [13]. Li-ion batteries are more portable and have a higher power density than other battery types. One of the best instances of a Li-ion BESS is the Hornsdale Power Reserve in Southern Australia, which is the largest such system in the world [14]. It stabilizes the electrical system by utilizing electricity from a nearby wind farm. Tesla built this 100 MW battery, which provides electricity to over 30,000 households. However, Li-ion batteries continue to face constraints that limit their application range [15]. One of the primary constraints is the effect of temperature on the LI-ion battery's reliability of operation. Typically, Li-ion batteries acceptable range of temperature is -20 to 60 °C [16]. However, 20-40 °C is the optimal working temperature range for Li–ion batteries, while the battery pack's local temperature difference of each battery should be less than 5 °C [17, 18]. Overheating and overdischarging can cause battery degradation, failure, and fire in the worst case scenario [19].

To obtain the optimum performance of battery electric energy storage, keep the battery temperature within the optimal range and enhance the temperature uniformity [20]. Extensive research efforts have recently been directed toward developing an advanced BTMS that can be classified as active or passive [20], direct or indirect [21, 22], series or parallel [23], cooling or heating [24], internal or external [25] air, liquid, phase change material (PCM) [26, 27], or hybrid [28]. Various kinds of cooling systems have their limitations and benefits. There are several things to consider while selecting the best BTMS, including capacity limits, installation costs, operational efficiency, and eco-friendliness. In order to bridge the gap between commercial manufacturers and researchers, new BTM tactics are constantly being examined. Recently, researchers have deemed the PCM to be the most effective. As a passive thermal control technique, BTMS PCM-based gives advantages, including low running costs and excellent temperature uniformity [29]. Because of its high temperature-control and temperature-stretching powers, PCM-based cooling has shown potential applications. However, the fundamental technological constraint preventing its practical applications due to low thermal conductivity performance [30]. Additionally, most commercial BTMS use air cooling [31], liquid cooling [32], and R134a indirect cooling [33] at the moment, and researchers are encouraged to work on a direct cooling method. Direct cooling has a higher heat transfer rate compared to indirect cooling due to the tendency of the contact surface between the pack and the coolant to absorb heat.

Despite indirect cooling, direct cooling absorbs the heat from the whole cell surface, which improves temperature uniformity by reducing the local heating impact at both positive and negative tabs [34]. Dielectric fluids with a high

combustion point, biodegradability, non-volatility, non-toxicity, and higher thermal conductivity might be regarded as viable BTMS coolants and for other high heat flux devices. Additionally, high chemical stability, non-toxicity, non-flammability, etc., must be considered for safety and health concerns. Due to their non-conductivity, dielectric fluids interact directly with the battery wall, which increases the surface area available for heat control [35]. Since dielectric cooling technology eliminates the need for a secondary or indirect cooling system, it makes BTMS more simple by reducing the complexity of such systems [36]. Van Gils et al.[34] experimentally investigated the pool boiling cooling efficiency by immersing a cell in Novec 7000 (a dielectric liquid manufactured by the American company 3M). According to their findings, even without boiling, the fluid's cooling capability was far greater than that of air. They observed a temperature difference of around 0.7 °C between the negative and positive tabs of the cell in the non-boiling domain, but this difference vanished when the liquid around the cell began to boil. Mahesh et al. [37] explored the Li-ion battery and battery pack direct cooling performance characteristics for electric cars utilizing immersion cooling with different dielectric fluids. The maximum temperature at the positive tab of a pouch cell submerged in dielectric fluid flow facilitated by tab cooling was reduced by 46.8 percent when compared to spontaneous convection at a discharge rate of 3 C, indicating superior cooling performance. Jithin and Rajesh [38] numerically investigated the thermal management of Li-ion battery using various dielectric liquids, including mineral oil, deionised water, and AmpCool AC-100 (AmpCool). They discovered that all dielectric fluids efficiently restrict temperature rise to less than 5 °C during 2 C discharging operation.

Typically, the choice of dielectric media has been limited to solids, liquids, gases, and vacuum. There is a wide range of applications that suffer from this limited choice of dielectric materials, especially for any application that requires a combination of withstanding strong electric fields, dissipating heat efficiently, and allowing for fast motion. Traditional dielectric media lack at least one of these three requirements. However, it has been recognized that super-critical fluids have the potential to satisfy all these criteria since they combine high dielectric strength, low viscosity, and excellent heat transfer capabilities [39]. sCO_2 as a dielectric medium is considered an ideal working fluid to respond to the growing concerns over environmental pollution and insufficient energy conversion efficiency because of its favorable properties, including high dielectric strength, a non-flammable nature, compressibility, a plentiful reserve, zero ozone depletion potential, non-toxicity, low cost, and a low risk of global warming. sCO_2 is easily achievable since its critical pressure is just 7.4 MPa and its critical temperature is only 31.1 °C, which is very close to ambient

Table 1: Energy storage system characteristics (source: The World Energy Council)

Name of ESS	Maximum power (MW)	Discharge time	Max cycles or lifetime	Energy density (W/H-liter)	Efficiency
Hydro pumbped	3000	4-16 hours	$30-60$ years	$0.2-2$	$70-85\%$
Compressed air	1000	2 -30 hours	$20-40$ years	$2-6$	$40-70\%$
Li ion battery	100	1 min - 8 hours	$1000-10000$	$200-400$	$85-95\%$
Molten salt (thermal)	150.0	many hours	30 years	$70-210$	$80-90\%$
Lead-acid battery	1000	1 min - 8 hours	$6-40$ years	$50-80$	$80-90\%$
Hydrogen	100	minutes-week	$5-30$ years	600	$25-45\%$
Flow battery	100	many hours	$12000-14000$	N/A	N/A
Flywheel	20	seconds - minutes	20000 – 100000	20 – 80	$70-95\%$

Table 2: Technical specifications of Li-ion

battery cell.

Contents	Battery size	Mass	Rated capacity	Rated voltage	Charge/discharge voltage
Value	$16 \times 65 \times 131\ \left(\mathrm{mm}^3\right)$	328 (g)	20 (Ah)	3.3 (V)	$3.65/2.0$ (V)

temperature. The dielectric characteristic of sCO_2 comprehensively studied by Jia Wei [39] in his PhD dissertation. Electrical breakdown experiments show that the dielectric strength of pure sCO_2 is around 250 kV/mm, indicating that supercritical is an excellent dielectric medium. However, the pump's power consumption, which is parasitic for all forced mediums, and relatively high working pressure limit its application as a cooling medium for compact devices. Forced cooling techniques, such as forced air cooling, water cooling, and sCO_2 cooling, nearly inevitably require peristaltic pump power. Adjusting the fluid flow inlet parameters closer to the critical point, however, can minimize the pump power consumption of sCO_2 fluid by improving heat transfer and thus decreasing the mass flow rate.

As mentioned above in the literature about large-scale BESS accidents [40], it is important to design a proper thermal management system to avoid such accidents and achieve optimum performance of the BESS. According to the literature, there is a significant amount of research available on battery thermal management, but relatively little research has been done on large-scale BTMS. In this study, a large-scale battery pack of 20×5 Li-ion batteries is designed for BESS applications, and a structurally optimized BTMS with sCO_2 as a coolant agent is used. The cooling performance of sCO_2 is compared with that of two conventional fluids: AmpCool and mineral oil. The effects of different fluid media, various numbers of fluid inlets, different discharge rates, and an increasing number of mass flow rates are numerically explored. Performance evaluation criteria (PEC) and the Fanning friction factor were introduced as indicators to fully consider both heat transfer performance and pressure loss.

2. Model description and solution

In this section, physical modeling, formulation of computational fluid dynamics, boundary conditions, and data reduction and evaluation are comprehensively described.

2.1. Physical model

A proper BTMS is required to guarantee the operation of the Li-ion batteries at a suitable temperature range in order to avoid accidents in BESS. In this study, a 100-battery pack of BTMS is designed for the application of BESS. The prismatic $LiFePO_4$ battery cells with a capacity of 20 Ah (single cell) are modeled in a structure-optimized configuration with a total voltage of 330 V. The single battery dimensions are $16 \times 65 \times 131\ mm^3$, with the tabs having a diameter of 6 mm and a height of 8 mm, as shown in Table 1. The battery module with BTMS has an overall dimension of $131 \times 337 \times 446\ mm^3$. There are a maximum of 9 inlets and 9 outlets with the same dimension of $6 \times 6\ m^2$, and the entrance and exit pipe is extended to 50 mm. The intake segment ensures the flow is fully developed before hitting the heated area, while the exit section prevents backflow. The width of the cooling system and the gap between the horizontal cells are 6 mm, while the vertical cells are adjacent. Figures 1(a) and (b) show the single-cell battery and 100-battery pack with the proposed sCO_2 fluid cooling technology. The thermophysical properties of batteries, BTMS, and cooling fluids are shown in Table 3. The ability of a substance to conduct heat is measured by its thermal conductivity, which is an essential characteristic/property of a material. Because of its layered structure and the existence of chemical processes, the thermal conductivity of Li-ion prismatic cells is significantly orthotropic. In a Li-ion prismatic cell, the active zone's orthotropic thermal conductivity matrix is represented by the following equations:

$$k_{cell} = \begin{bmatrix} k_{\text{trans}} & 0 & 0 \\ 0 & k_{\text{planar}} & 0 \\ 0 & 0 & k_{\text{planar}} \end{bmatrix} = \begin{bmatrix} 0.9 & 0 & 0 \\ 0 & 2.7 & 0 \\ 0 & 0 & 2.7 \end{bmatrix} \tag{1}$$

Moreover, by minimizing the complication of indirect cooling and eliminating thermal contact resistance losses, the proposed idea enabled direct-contact cooling for large battery surfaces.

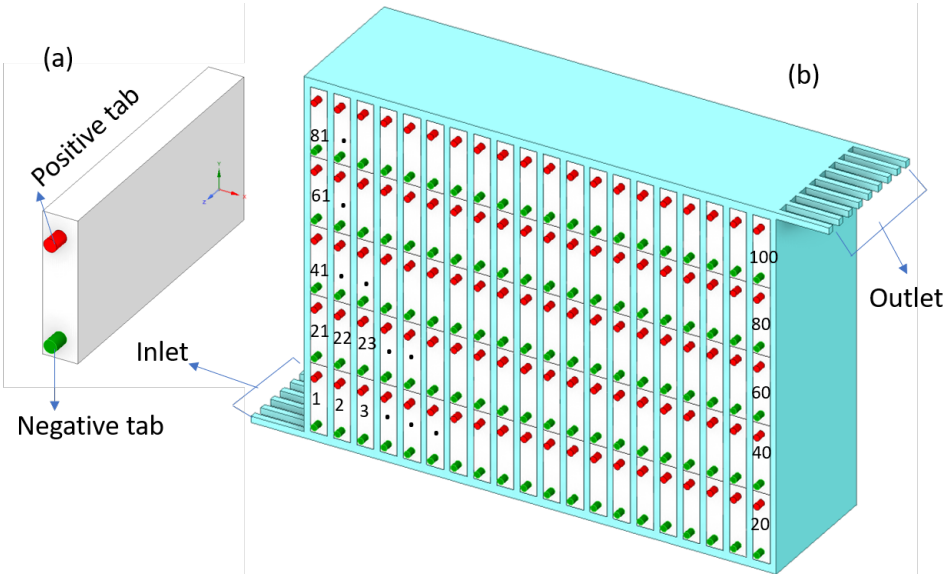

Figure 1: Schematic diagram: (a) Single battery cell (b) 100 battery pack with thermal management system

2.2. Formulation of computational fluid dynamics

To evaluate the BTMS's cooling performance, it is necessary to map out the system's flow field and temperature field. The Computational Fluid Dynamics (CFD) approach is a powerful tool for calculating the flow and temperature fields. To investigate the thermal performance of the BTMS, the CFD approach is used with three different working fluids: mineral oil, AmpCool, and sCO_2. The Reynolds number is used to to determine the nature of the flow. At a constant mass flow rate, the flow of mineral oil and AmpCool is laminar, whereas the flow of sCO_2 fluid is turbulent. All calculation results depicted in this paper are under steady-state conditions. For turbulent flow, the energy equation and Shear Stress Transport (SST) k-ω turbulent model are used, while for laminar flow, a simple laminar algorithm is employed. The NIST Standard Reference Database 23, version 9.0 software is used to calculate all thermo-properties for sCO_2, including density, thermal conductivity, specific heat, and viscosity, as shown in Figure 2 [41]. The second-order upwind approach solves the continuity, momentum, and energy equations by coupling the pressure and velocity terms in the momentum equation using the SIMPLE algorithm. To reduce the linearization error, the convergence criterion for the normalized residual of individual governing equations was specified to be less than 1.0×10^{-6}.

2.3. Boundary conditions

The inflow boundary conditions for mineral oil and AmpCool are 0.0036 kg/s at ambient pressure. The heat generated source for each battery cell is considered 28105 W/m^3 at 1 C discharged rate [42]. The environmental

Table 3: Material properties used in present study.

Parts	Density$(\mathrm{kg/m^3})$	T. conductivity$(\mathrm{W/mK})$	Specific heat(J/kgK)	Viscosity$(\mathrm{kg/ms})$
Battery cells	2810	Eq. 1	733	/
Battery box	7930	16.3	500	/
Mineral oil	924	0.13	1900	0.05
AmpCool	811	0.1373	2203.2	0.008
sCO_2	Ref. [41]	Ref. [41]	Ref. [41]	Ref. [41]
Pos. tab	8110	16	520	/
Neg. tab	8400	110	385	/

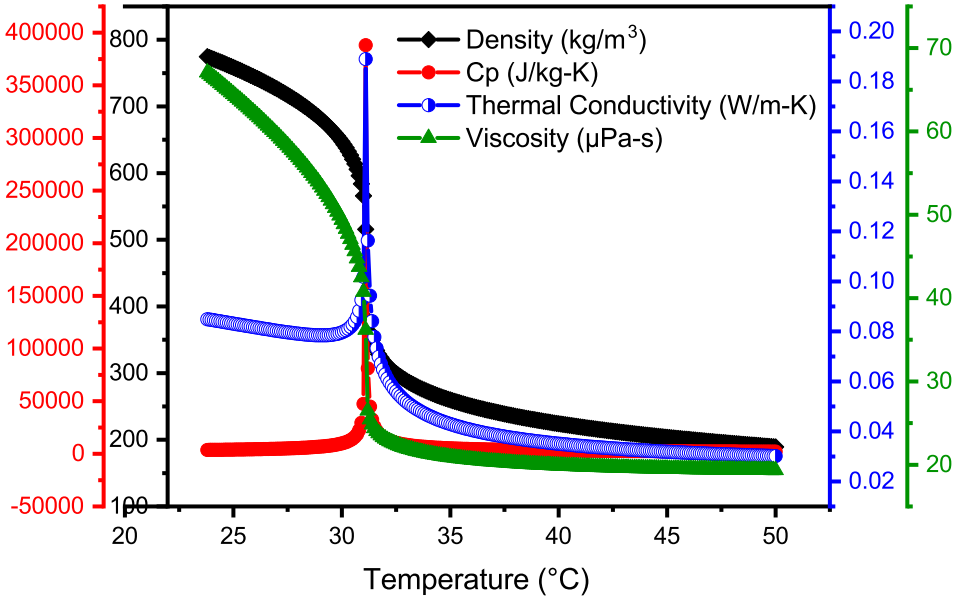

Figure 2: Thermophysical properties of supercritical CO_2.

temperature and natural heat transfer coefficient are 30 °C and 5 $Wm^{-2}K^{-1}$, respectively. In the case of sCO_2, before permitting it to flow in the inlets, the sCO_2 is considered in a chamber at 7.4 MPa supercritical pressure. The given inlet mass flow rate conditions are 0.0018, 0.0036, and 0.0054 kg/s. The channel outlets are assigned a pressure outlet condition, and the gauge pressure is set at 0 Pa. The outside walls of the fluid cold plate are meant to be adiabatic. A no-slip boundary condition is given for the fluid cooling plate-channel contact, and contact resistances between distinct regions are neglected.

2.4. Data reduction and evaluation

The primary objective of this section is to evaluate the BTMS thermal performance in terms of average heat transfer coefficients, average Nusselt number, Fanning friction factor, power consumption, and performance evaluation criteria using the following equations.

The local heat transfer coefficient and Nusselt number are expressed as:

$$HTC_n = \frac{q_n}{T_{ave,n} - T_b} \tag{2}$$

$$Nu_n = \frac{HTC_n \times D_h}{\lambda_f} \tag{3}$$

where $n = 1, 2, 3, ...100$, q_n, $T_{ave,n}$, T_b, D_h, and λ_f denote the number of battery pack cells, average wall heat flux, battery average wall temperature (T_{ave}), bulk temperature T_b, hydraulic diameter of the channel, and fluid thermal conductivity, respectively. The battery pack's overall averaged heat transfer coefficient and Nusselt number are defined as [43]:

$$HTC_{ave} = \frac{\sum_{n=1}^{100} HTC_n}{n} \tag{4}$$

$$Nu_{ave} = \frac{\sum_{n=1}^{100} Nu_n}{n} \tag{5}$$

The following Fanning friction factor, f, and power consumption equations are used to quantify the pressure drop:

$$f = \frac{2 \times \Delta P_{ave} \times D_h}{\rho \times u_{ave}^2 \times L} \tag{6}$$

$$\text{Power } = \Delta P \cdot \dot{V} \tag{7}$$

where $\Delta P = P_{\text{in},ave} - P_{\text{out},ave}$ and $\dot{V}$ denotes the average pressure drop and volume mass flow rate. ρ, u_{ave}, and L present the density of the fluid, the overall average velocity, and the length of the BTMS channel (inlet and outlet channel length are equal). The optimum design for BTMS cooling systems can be determined by evaluating performance evaluation criteria (PEC). BTMS cooling PEC in terms of heat transfer and pressure loss is defined as:

$$PEC = \frac{(Nu/Nu_0)}{(f/f_0)^{1/3}} \tag{8}$$

where Nu_0 and f_0 are the Nusselt number and Fanning friction factor of the AmpCool, respectively.

3. Results and discussion

3.1. Experimental validation and Grid independence analysis

It is discussed in the above literature that no supercritical BTMS has yet been established; therefore, the simulation work is validated with air cooling and sCO_2 pipe cooling experimental results [42, 44]. Figure 3(b) depicts the maximum temperature profile of simulations and the experimental findings of air cooling. Each battery has two measuring locations. The battery temperatures in the simulation model are measured in the same position as in the experiment.

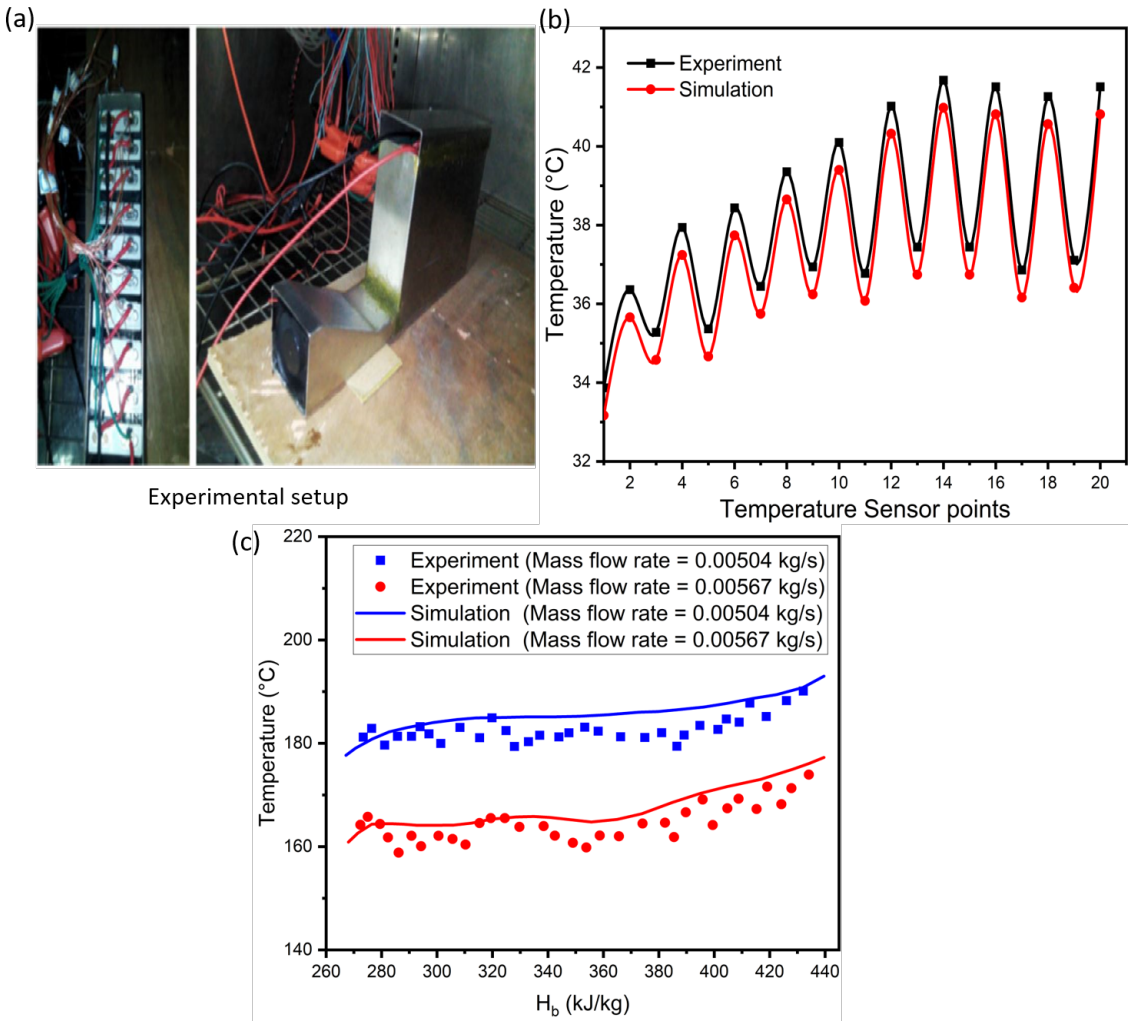

Figure 3: Temperature comparison: (a) Experimental setup [42] (b) validation of simulation results with an air cooling experiment (c) simulation validation using sCO_2 experimental results at various mass fluxes [44].

The maximum temperature of the battery pack in the models closely corresponds to that observed in the experiments.

Since the heat generation rate of the batteries increases during charging/discharging processes in the experiment, the simulation graph line is somewhat below the experimental results because the heat-generating rate is assumed to remain constant during the simulation. The most noticeable difference between the simulation and experiment is merely 0.4 °C. In addition, the simulation work has also been validated using sCO_2 experimental results [44]. The SST k-ω turbulence model is used to simulate the wall temperature distribution at different mass fluxes, and the results are compared to those obtained in Guo's experiment [44].

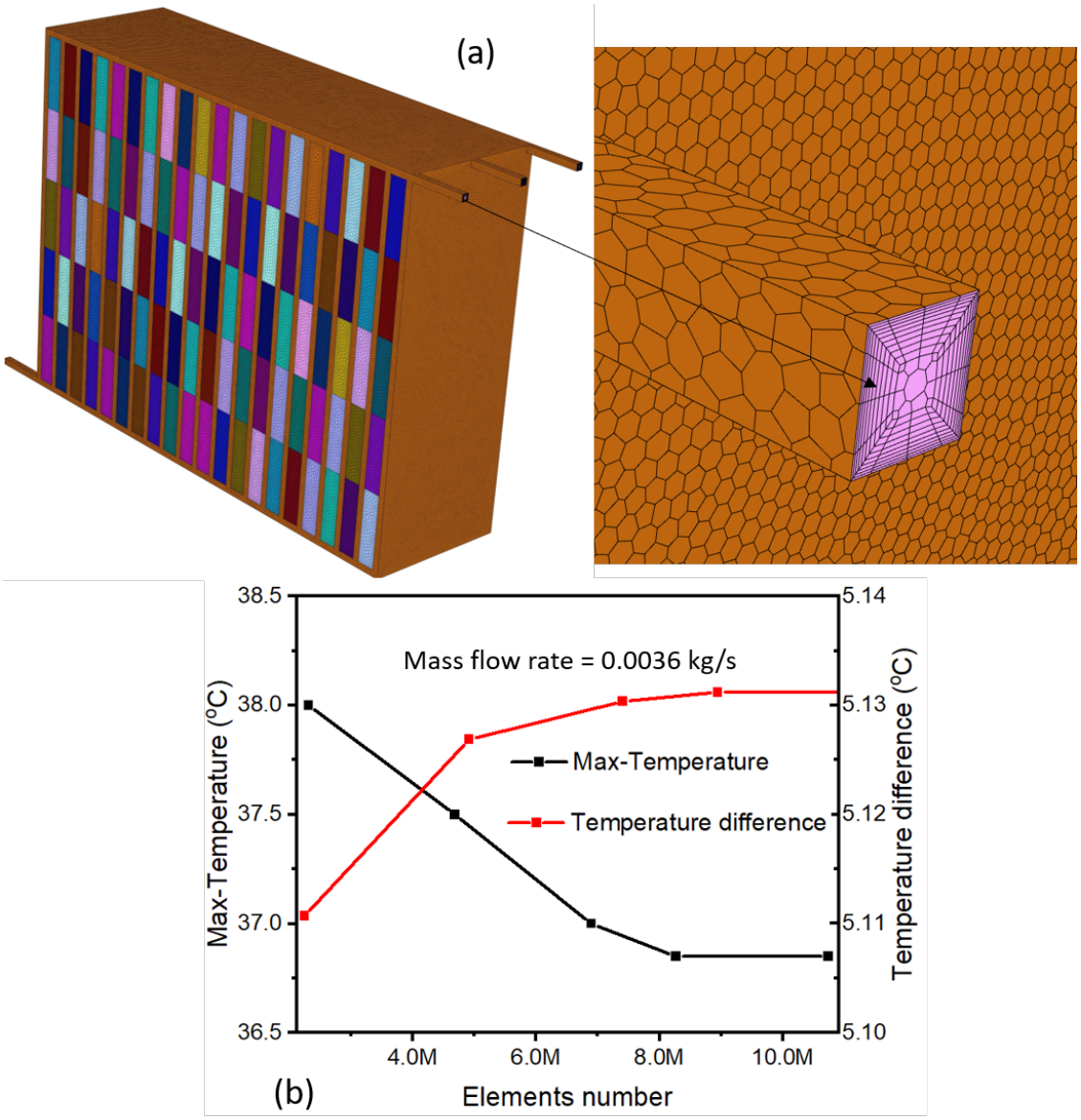

Figure 4: Mesh independence analysis: (a) polyhedral meshing (b) simulation result at varying grid number.

Figure 3(c) shows that the wall temperature in the heated tube does not remain constant in both the experimental

and simulated results at mass flow rates of 0.00504 kg/s and 0.00567 kg/s, respectively. The trends and magnitudes of the experimental results were accurately captured by the simulation wall temperature results. Based on the simulation and experimental results, it is concluded that the simulation results closely match the experimental data measurements.

The mesh quality has a huge impact on numerical outcomes. An accurate numerical simulation of turbulent flows requires mesh-independent grid considerations in order to achieve a reliable numerical result. The commercial software ANSYS Fluent 22.0 is employed for CFD simulations, and the battery pack is discretized by an unstructured polyhedral mesh using the Fluent meshing tool. The grid independence test is carried out using the SST $k-\omega$ model and sCO_2 fluid media. The simulation is conducted for five different grid sizes with an ambient temperature of 30 °C and an inlet mass flow rate of 0.0036 kg/s. As depicted in Figure 4(b), the overall size of the models converges to around 8,500,000 elements following grid dependence analysis because no variation in maximum temperature or temperature difference appeared after increasing the number of elements.

3.2. Comparison of supercritical CO_2 with conventional fluids

This section investigates the effect of three different fluid media: AmpCool, mineral oil, and sCO_2 at three fluid inlets. Figure 5 depicts the temperature variation, average heat transfer coefficient, and Fanning friction factor of an immersion-cooled battery pack at a mass flow rate of 0.0036 kg/s. As presented in Figure 5(a), the highest temperature of the battery module is 95 °C recorded for the mineral oil at 1 C-rate. Mineral oil and AmpCool effectively drop the maximum temperature profile of the first 30 batteries, and the batteries straighten to the inlets. The AmpCool dielectric liquid outperforms mineral oil in reducing the temperature of the battery pack, but the maximum temperature of 80 °C still does not appear to be friendly. In both cases of AmpCool and mineral oil, the temperature difference of the majority of the batteries is greater than 8 °C. It has been discovered that AmpCool and Mineral Oil, which are regarded as the best immersion cooling solutions [38, 20, 37], fail to cool a large battery pack system. Therefore, an efficient and environmentally friendly cooling system is needed. The sCO_2 fluid, which is environmentally friendly and easily achievable [45], is considered to be capable of controlling such extreme temperatures. As illustrated in Figure 5(a), sCO_2 restricts the battery module temperature to 37 °C. Because of its higher diffusivity, lower viscosity, lower surface tension, and especially its high specific heat and thermal conductivity, sCO_2 outperforms AmpCool and mineral oil, particularly at the pseudo-critical point (T = 31.1 °C), where the specific heat is 200 and 174 times greater than that of mineral oil and AmpCool, respectively.

This can primarily be attributed to the more favorable thermophysical properties of the pseudo-critical region. Figures 5(a) and (b) show that, when compared to AmpCool and mineral oil, sCO_2 reduces the maximum temperature by 61% and 53%, respectively, and the temperature difference peaks at 61% and 56%, respectively. Figure 6 depicts the contours of AmpCool, mineral oil, and sCO_2, demonstrating that the temperature of the batteries straighten to the fluid inlets is lower due to low resistance to the fluid's velocity.

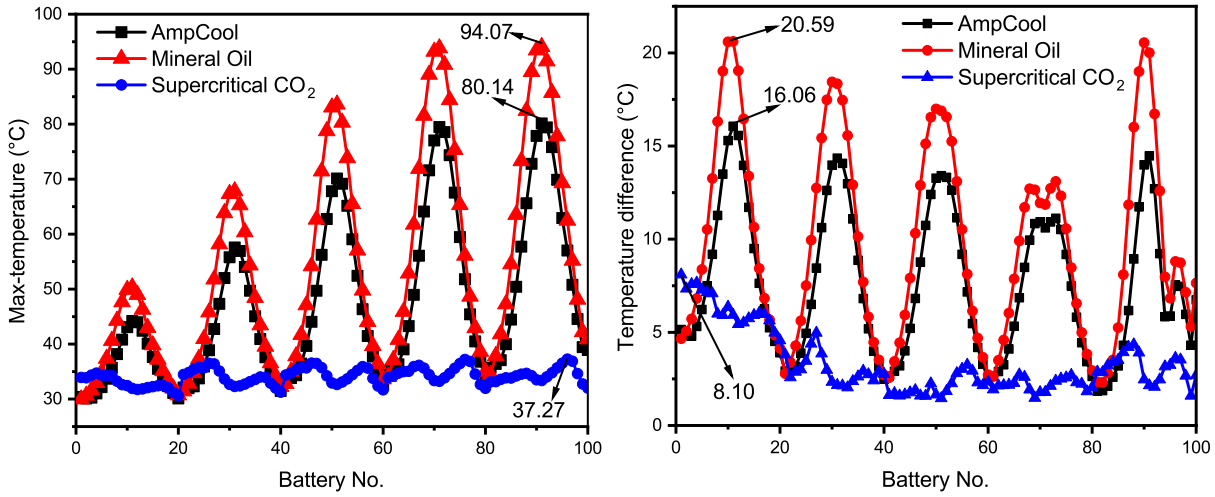

(a) Maximum temperature

(b) Temperature difference

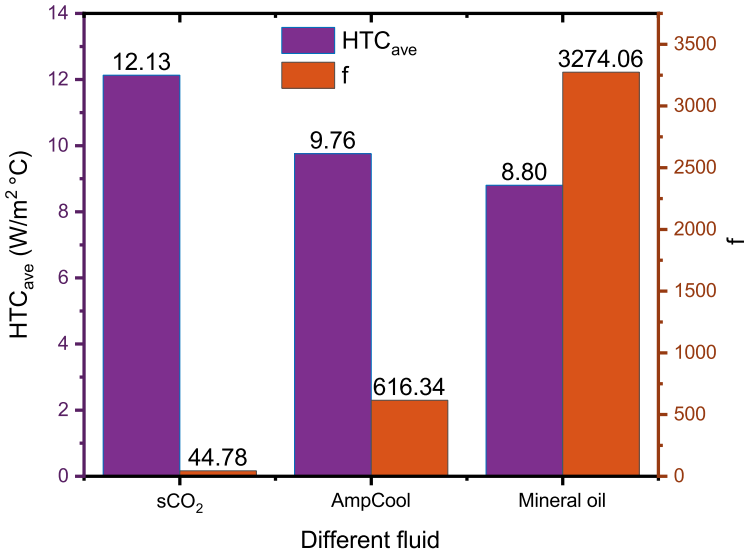

(c) Averaged HTC and Fanning friction factor

Figure 5: Comparison of the battery temperature and pressure drop at three fluid inlets (a) maximum temperature (b) temperature difference (c) averaged heat transfer coefficient and Fanning friction factor.

The average heat transfer coefficient and the Fanning friction factor for three fluid flow inlets at at 1 C discharge rate are compared. Figure 5(c) shows that the average heat transfer coefficient of sCO_2 outperforms AmpCool and

Table 4: Power consumption of different cooling fluids.

			Power consumption (W)		
Cases	No. of inlet	Mass flow rate (kg/s)	Mineral oil	AmpCool	sCO_2
1	3	0.0018	0.4749	0.0946	0.0092
2	3	0.0036	1.9298	0.4185	0.0622
3	3	0.0054	4.4161	1.0304	0.1915
4	5	0.0036	2.0594	0.4366	0.0654
5	9	0.0036	2.3669	0.4887	0.0592

mineral oil. The velocity of the fluid flow drops due to the higher viscosity and low diffusivity of the AmpCool and mineral oil, which increases the difference between the fluid and battery wall temperatures. In contrast, the velocity of the sCO_2 fluid flow increases due to lower viscosity and higher diffusivity, which results in a lower fluid and battery wall temperature difference. It can be noticed in equation 6 that the Fanning friction factor is dependent on the pressure drop, fluid density, and velocity of the fluid. The velocity and density of sCO_2 vary with temperature due to its compressible and supercritical nature. The averaged density of $496.8 kg/m^3$ has been calculated, which is lower than both AmpCool and mineral oil. Due to the higher density and higher viscosity of mineral oil (0.05 kg/m.s) and AmpCool (0.008 kg/m.s), the pressure drop is much higher than that of sCO_2. Table 4 compares the power consumption of the three fluids with varied mass flow rates and fluid flow inlets. It is very obvious from the results that as the mass flow rate increases, the power consumption increases due to a higher pressure drop. A sCO_2-based BTMS has the lowest power consumption among the three cooling fluids, which is much more energy efficient in cooling large-scale BESS than both AmpCool and mineral oil. The preceding discussion demonstrates that AmpCool and minerals have a significantly higher Fanning friction factor and a lower heat transfer coefficient than sCO_2, demonstrating that sCO_2 is the best coolant agent.

3.3. Different number of fluid inlets

The number of fluid inlets has a high impact on the Li-ion batteries' undesirable thermal behavior and pressure drop. Here, the effect of various numbers of fluid inlets on the battery module temperature has been investigated. Figure 7 depicts the maximum temperature, temperature difference, average heat transfer coefficient, and Fanning friction factor for three, five, and nine numbers of fluid flow inlets with a sCO_2 cooling fluid medium at a constant mass flow rate of 0.0036 kg/s and a constant 1 C discharge rate. The maximum temperature of the batteries fluctuates between 30 °C and 37 °C at three fluid flow inlets. Due to the low number of fluid inlets, the fluid density (496.8

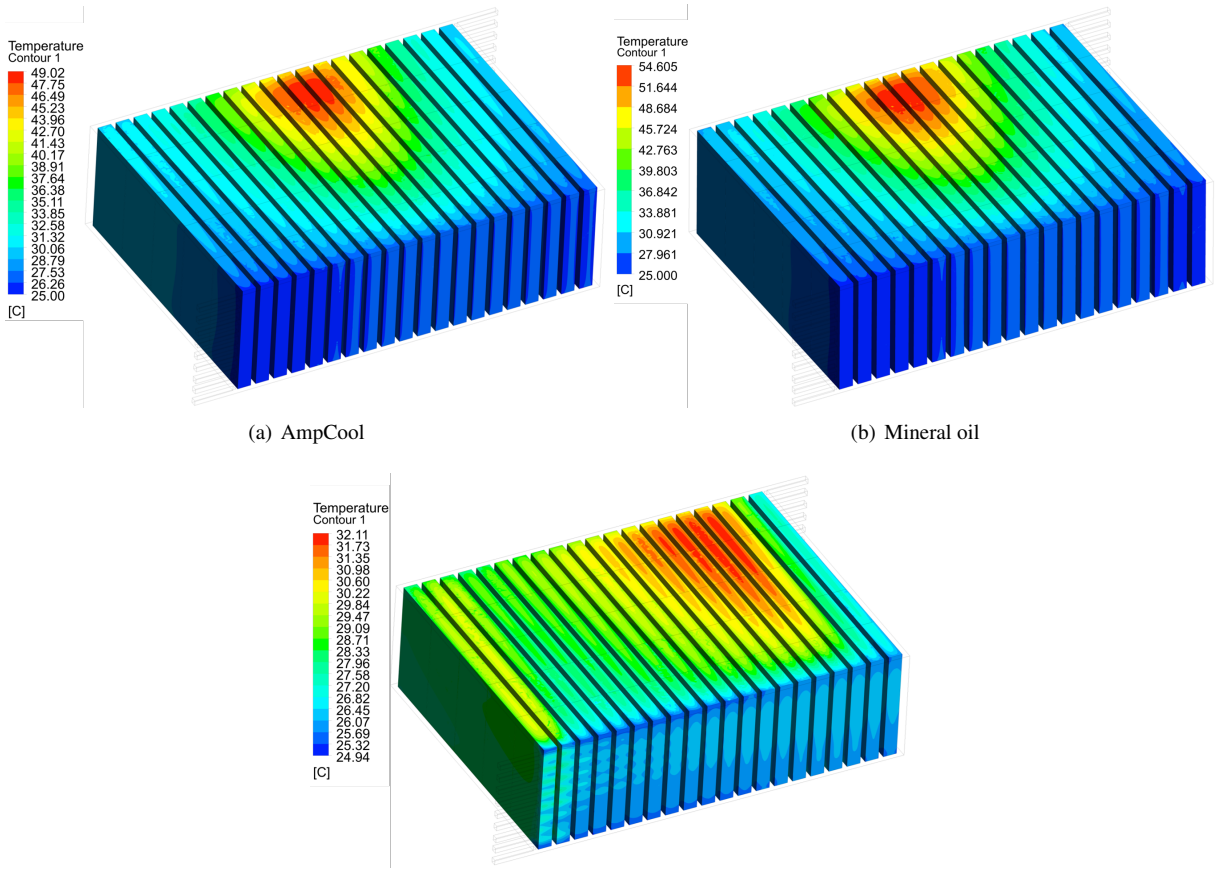

(a) AmpCool

(b) Mineral oil

(c) Supercritical CO_2

Figure 6: Contour of the maximum temperature at nine fluid inlets: (a) AmpCool (b) Mineral oil (c) Supercritical CO_2.

Table 5: Different simulation assumptions and results

Cases	No. of inlet	Mass flow rate (kg/s)	C-rate	T_{ave} (°C)	T_b (°C)	HTC_{ave} (kW/m^2 °C)	Nu_{ave}	Δ P	f	PEC
1	3	0.0018	1 C	34.47	31.19	10.48	90.341	5.09	44.78	5.04
2	3	0.0036	1 C	32.07	29.87	12.13	120.70	17.27	31.86	4.53
3	3	0.0054	1 C	30.05	28.83	13.33	145.20	35.47	26.16	4.49
4	5	0.0018	1 C	30.72	30.18	13.61	140.29	5.70	23.35	5.76
5	5	0.0036	1 C	29.82	29.29	14.49	171.18	18.15	16.79	5.05
6	5	0.0054	1 C	29.09	28.58	15.29	191.62	36.71	14.14	4.65
7	9	0.0018	1 C	29.62	28.78	14.79	172.05	5.87	8.50	5.76
8	9	0.0036	1 C	28.2	27.45	16.34	203.79	16.44	5.37	5.26
9	9	0.0054	1 C	27.39	26.78	17.32	225.01	38.85	5.62	4.71
10	9	0.0036	2 C	29.84	28.96	28.85	326.41	19.71	6.63	7.94
11	9	0.0036	3 C	31.35	29.9	39.64	465.80	20.62	6.89	11.18

kg/m^3) and diffusivity are low; thus, the maximum temperature approaches 37 °C. The first twenty battery cells in the module have the highest temperature difference. This is due to a low fluid inlet number, in which the fluid crosses the bottom of the batteries with a relatively high velocity. As a result, the bottom half of the first twenty batteries had a relatively low temperature, as shown in the contour in Figure 6. The remaining batteries have a temperature difference of less than 6 °C, which is close to the optimal temperature difference.

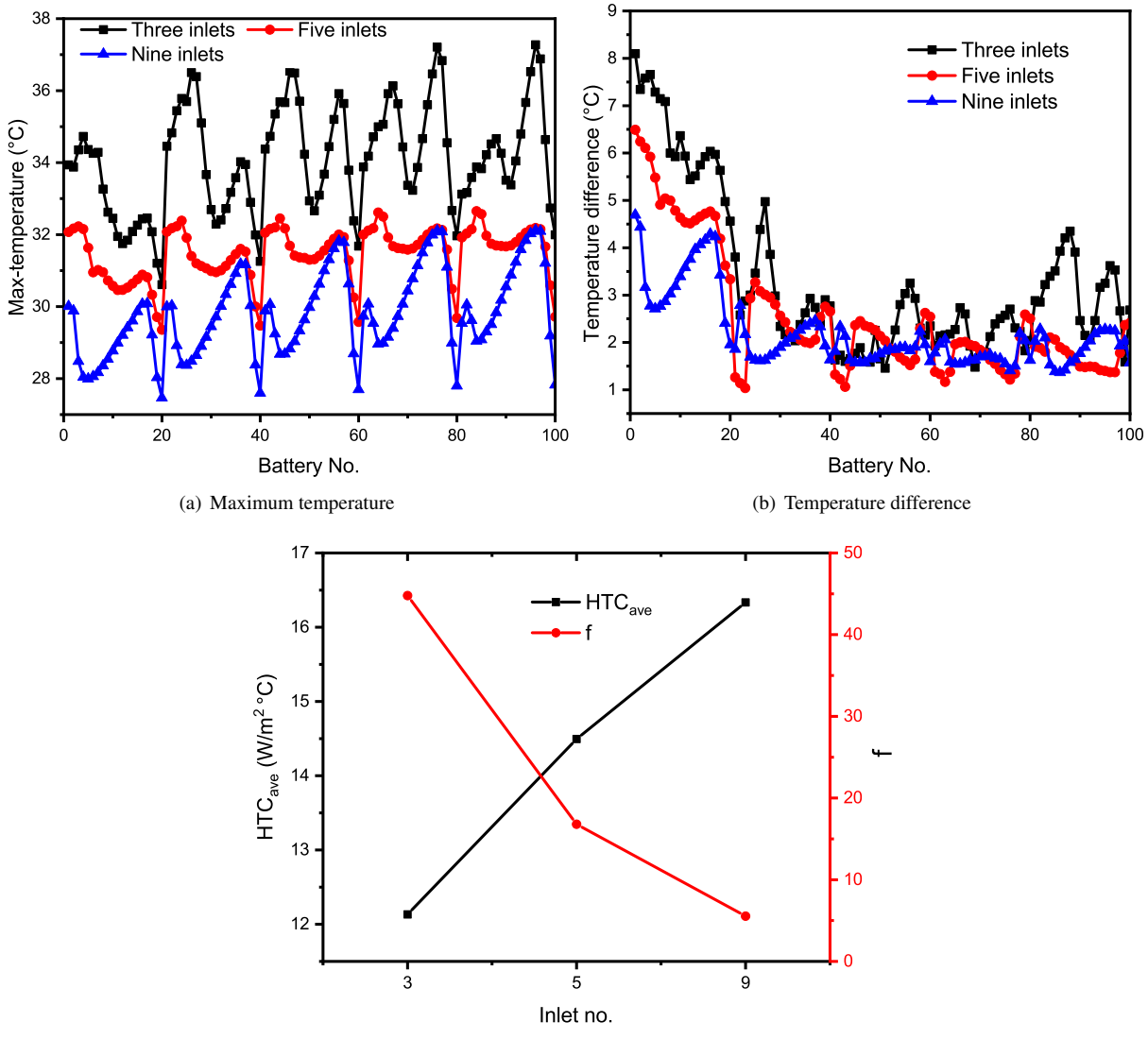

(a) Maximum temperature

(b) Temperature difference

(c) Averaged HTC and Fanning friction factor

Figure 7: Comparison of the battery temperature at different number of fluid inlets (a) maximum temperature (b) temperature difference (c) averaged heat transfer coefficient and Fanning friction factor.

The number of inlets in the sCO$_2$-based BTMS has been increased to five and nine for further improvement. The increasing number of fluid inlets allows more fluid to enter, which raises the density and average velocity of

sCO_2 and allows it to be easily diffused over a vast region of the batteries. As a result, the maximum temperature and temperature deference were reduced with five inlets compared to three inlets, as illustrated in Figure 7 (a). The maximum temperature of the battery module was dropped to 32.6 °C, and temperature mitigation has been improved. The temperature difference for the first 20 batteries in the pack has been maintained between 6.5 °C and 3.5 °C, while the remaining batteries range between 3 °C and 1 °C (Figure 7b). The temperature difference of some batteries at five inlets is still above the optimum; therefore, the number of inlets has been increased. The sCO_2 performs admirably with nine fluid inlets, owing to further improvements in the fluid's density (714.25 kg/m^3), diffusivity, and average velocity. The maximum temperature of the batteries ranges from 26 to 32 °C (Figure 7a), with a temperature difference of 4.5 °C for the first twenty batteries and 1.5 to 3 °C for the remaining batteries (Figure 7b). Moreover, an enhanced heat transfer coefficient owing to an increase in the number of cooling fluid inlets is due to the availability of a larger inlet area for heat transfer, as shown in Figure 7(c); this is explained in detail by considering the surface area coverage parameter [46]. The increased number of fluid flow inlets from three to nine enhances the fluid density and velocity, resulting in an increasing heat transfer coefficient and pressure drop and a decreasing Fanning friction factor, as can be seen in Table 5 and Figure 7(c). The highest average heat transfer coefficient of 16.34 W/m^2 and lowest Fanning friction factor of 5.54 are observed at nine fluid inlets, which clearly indicates the optimum point considering inlet number.

3.4. Different discharge rate

The heat generated by the battery pack was routed to the sCO_2-based cooling system, and the temperature variation of the battery modules was thoroughly investigated in the following analysis with nine fluid flow inlets. It is self-evident that the high rate of discharge causes the batteries to generate more heat. Power-hungry operations are likely to increase the discharge C-rate in rechargeable battery-powered devices. Temperature rise is the thermal impact of ohmic heating caused by the discharge C-rate, which accelerates the degradation of Li-ion batteries. As the discharge C-rate exceeds a certain limit, the battery's internal temperature rises, which places additional strain on the battery, shortens its lifespan, and hastens its capacity loss. Therefore, sCO_2-based BTMS is employed to maintain the battery pack's undesirable temperature rise at high discharge rates within an optimum range. Figure 8 shows that the maximum temperature and temperature difference increase as the C-rate increases. The increasing discharge rate increases the battery cell's internal resistance, which results in a temperature rise. As shown in Figure 8(a), at 1 C, the maximum

temperature is 31 °C and the highest temperature difference is 4.5 °C, whereas at 2 C, the maximum temperature is 34.6 °C and the temperature difference is 6.5 °C. The temperature at 2 C is gradually decreasing to 3 °C until battery 20 and then fluctuating between 3 and 1 °C for the remaining batteries. Similarly, the maximum temperature and temperature difference follow the same trend at 3 C, and only a 2 °C increase is observed compared to 2 C.

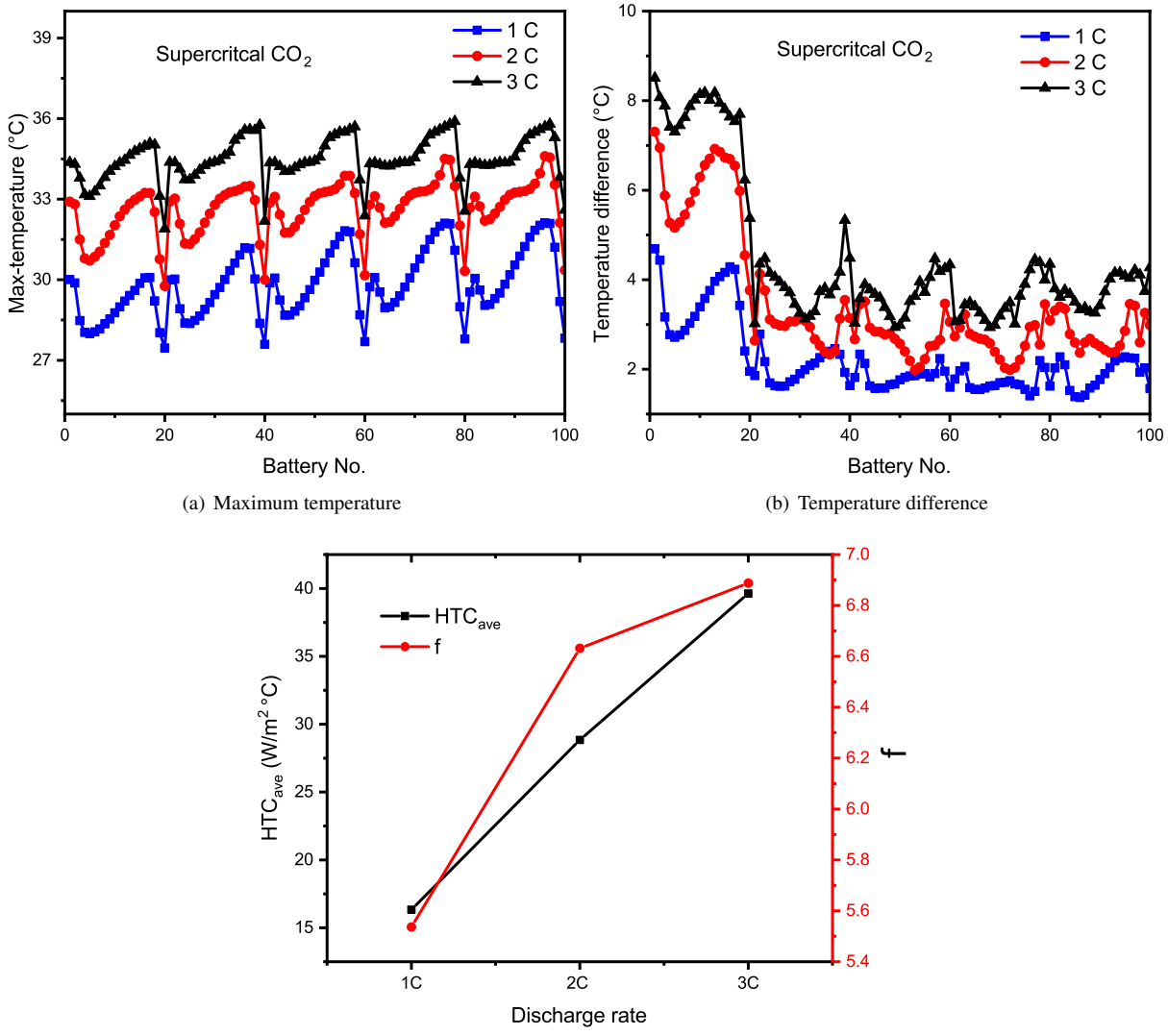

(a) Maximum temperature

(b) Temperature difference

(c) Averaged HTC and Fanning friction factor

Figure 8: Comparison of the battery temperature at different discharging rate with nine number of fluid inlets (a) maximum temperature (b) temperature difference (c) averaged heat transfer coefficient and Fanning friction factor.

Figure 8(c) depicts the average heat transfer coefficient and Fanning friction factor at various discharge rates. For CO_2 at supercritical pressures, the batteries' wall temperature increases with increasing discharge rate and approaches the pseudo-critical temperature, resulting in enhanced heat transfer. It is due to the specific heat capacity of the sCO_2

fluid near the batteries' walls rising, further enhancing heat transfer between the sCO_2 and the wall. The average temperature of sCO_2 at 1 C near the batteries' walls is far from pseudo-critical, resulting in a lower volume average specific heat capacity (5710.8 J/(kg K)), which contributes to a lower heat transfer coefficient. Moreover, with the increased discharge rates of 2 C and 3 C, the average battery wall temperature and fluid volume average temperature increased due to high heat generation, with the fluid volume average temperature approaching the pseudo-critical point, as shown in Table 5. This results in increased specific heat capacities of 66700.5 J/(kg K) and 132990.9 J/(kg K) at 2 C and 3 C, respectively, causing heat transfer enhancement. Furthermore, as the discharge rate increases, the sCO_2 temperature rises, causing the fluid density to fall and the velocity to rise, resulting in a slight increase in the Fanning friction factor. Based on the above explanation, it is concluded that sCO_2 is capable of regulating the temperature of the BESS to an optimal range at a high discharge rate.

3.5. Impact of mass flow rate

The impact of sCO_2 mass flow rate at a constant discharge rate (1 C) and constant ambient temperature (25 °C) is discussed in this section. Figures 9(a) and (b) depict the maximum temperature and temperature difference profiles of the battery module as the mass flow rate increases. The increasing mass flow rate increases the turbulent intensity of sCO_2 and the Reynolds number, resulting in a stronger turbulence flow inside the tube, which reduces the temperature profile. Figure 9(a) shows that the maximum temperature reaches 34 °C, 32 °C, and 31 °C for mass flow rates of 0.0018 kg/s, 0.0036 kg/s, and 0.0054 kg/s, respectively. The increasing mass flow rates have an impact on the temperature uniformity; as the mass flow rate increases, the temperature difference decreases. At 0.0018 kg/s, 0.0036 kg/s, and 0.0054 kg/s, the temperature difference of the first 20 batteries varies between 6 °C and 4 °C, 4.6 °C and 2 °C, and 3.8 °C and 1.8 °C, respectively. Meanwhile, the remaining batteries' temperature difference ranges between 2.5 and 1.1 °C. In addition, due to the compressible and supercritical nature of sCO_2, its density and diffusivity increase with increasing mass flow rate and decreasing temperature. As a result, sCO_2 cooling performance is enhanced at high mass flow rates. The average heat transfer coefficient increases from 14.7 to 17.3 W/m2 °C as the mass flow rate of sCO_2 increases (Figure 9c). This is primarily due to boosting turbulence intensity as sCO_2 mass flow rate increases. Increased turbulence intensifies fluid mixing, which improves heat transfer between the fluid and the battery wall. This explains why heat transfer coefficients for constant-property fluids increase with mass flow rate. Furthermore, the increasing mass flow rate enhances the pressure drop, as can be seen in Table 5. This is mainly due to the fact that

the Reynolds number increases with an increasing mass flow rate. The Fanning friction factor drops to 5.54 at 0.0036 kg/s and slightly increases at 0.0054 kg/s to 5.62. This is due to the huge impact of temperature on sCO_2 density. The difference in maximum temperature at mass flow rates of 0.0036 and 0.0054 kg/s is very small, therefore the density increment is comparatively lower at 0.0054 kg/s, which results in a slight increase in the Fanning friction factor.

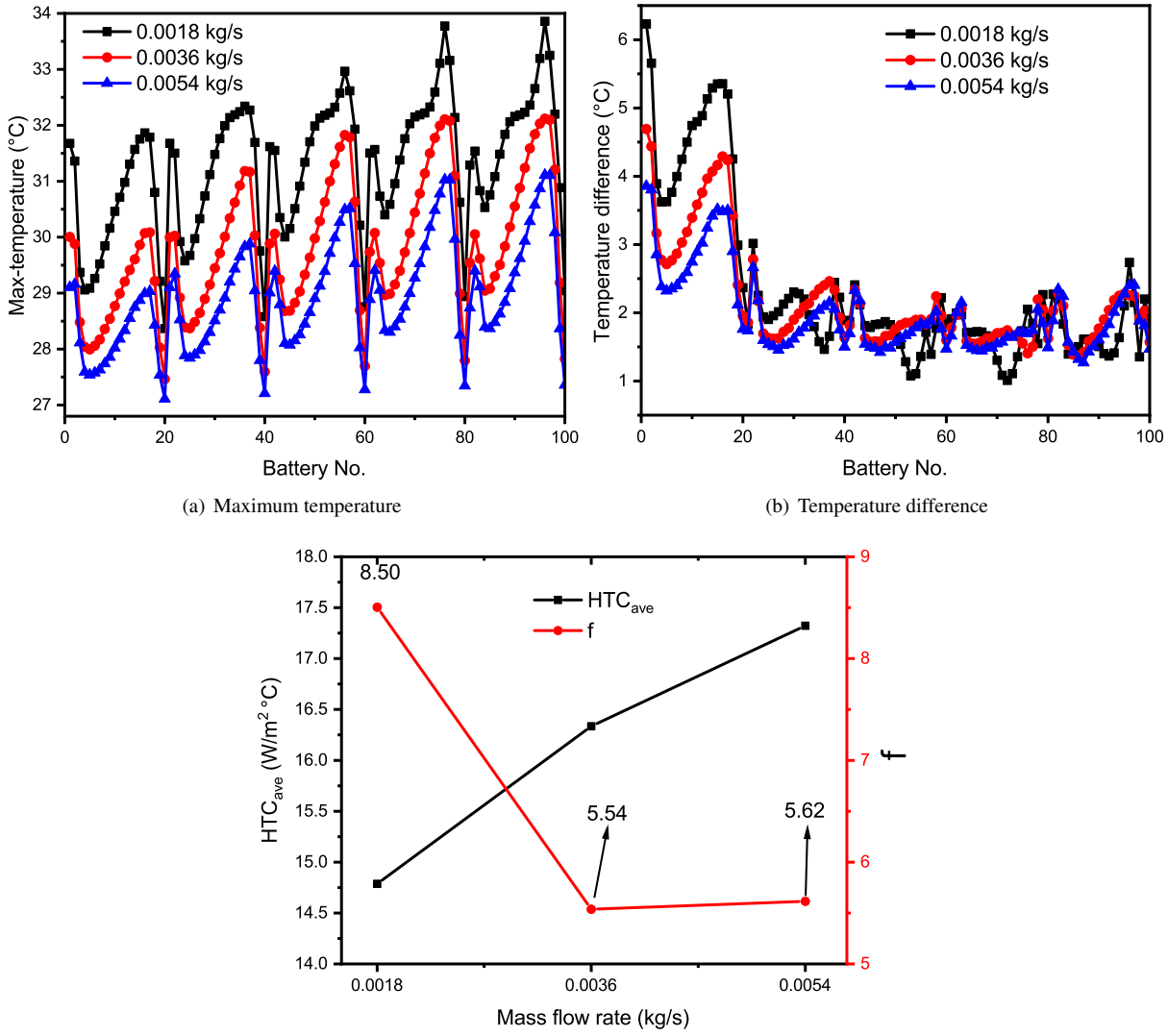

(a) Maximum temperature

(b) Temperature difference

(c) Averaged HTC and Fanning friction factor

Figure 9: Comparison of the battery temperature at different mass flow rates with fluid medium (a) maximum temperature (b) temperature difference (c) averaged heat transfer coefficient and Fanning friction factor.

3.6. Heat transfer performance evaluation

The heat transfer PEC of a novel sCO_2 BTMS with increasing mass flow rate and number of fluid flow inlets is investigated in this section. Figure 10 shows that all cases exhibited PEC greater than 1, indicating that at three, five,

and nine inlets, the overall cooling performance of the BTMS could be improved under all the investigated mass flow rates. This means that, despite the fact that all cases resulted in a pressure drop, the heat transfer enhancement could benefit the novel BTMS. The heat transfer PEC is boosted at increasing fluid inlets due to a significant improvement in the Nusselt number and a decrease in the Fanning friction factor.

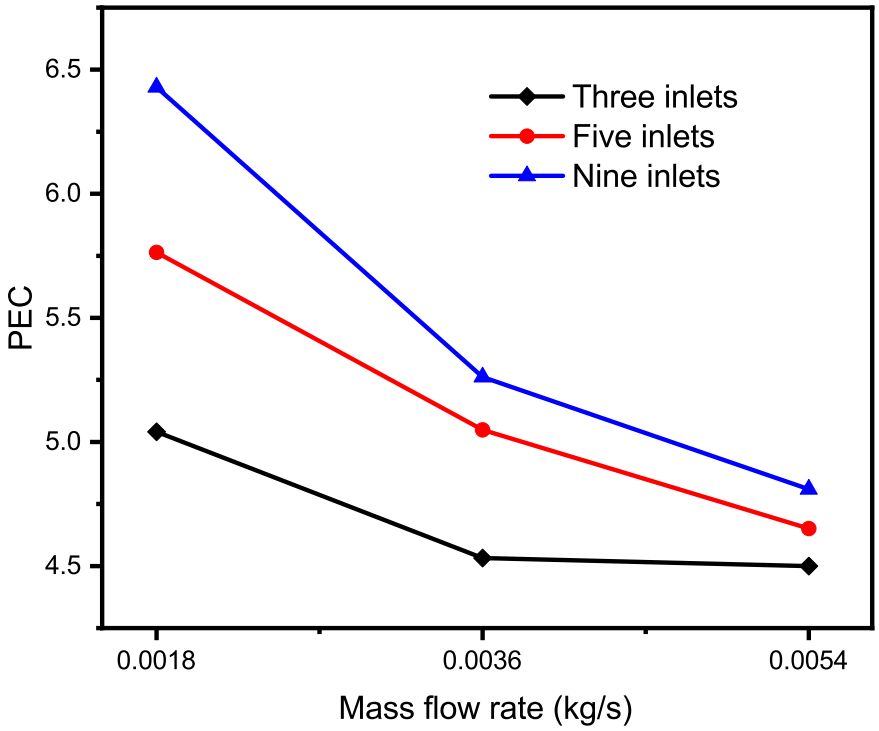

Figure 10: Heat transfer performance evaluation criteria with increasing mass flow rate of sCO_2 at different number of fluid inlets.

Furthermore, as the mass flow rate increases, the PEC decreases due to significant pressure loss. The nine-inlet BTMS continuously achieved the highest PEC at the investigated mass flow rates, outperforming the five-inlet BTMS by 0.71, 0.21, and 0.06, and outperforming the three-inlet BTMS by 1.4, 0.72, and 0.21. As a result, when weighing the trade-offs between cooling performance and the Fanning friction factor in the design of BTMS with various fluid flow inlets, the nine-inlet BTMS may be the best option among all cases.

4. Conclusions

In this study, a novel strategy is utilized to control the undesirable temperature rise in a 100-battery pack using sCO_2. The influence of different fluid media, various numbers of fluid inlets, coolant mass flow rate, and different

discharge rates on the thermal behavior of the battery module at a constant ambient temperature is numerically investigated. The major findings are summarized below:

- The sCO_2 outperforms AmpCool and mineral oil due to its higher diffusivity, lower viscosity, lower surface tension, and especially its high specific heat and thermal conductivity, particularly as temperature approaches the pseudocritical point, where the specific heat is 200 and 174 times greater than that of mineral oil and AmpCool, respectively. The sCO_2 mitigates the maximum temperature peak by 61% and 53%, respectively, and the temperature difference by 61% and 56%. In addition, sCO_2 outperforms AmpCool and mineral oil in terms of average heat transfer coefficient and friction factor.

- The maximum temperature and temperature differential decrease dramatically as the number of fluid inlets increases. The increased number of fluid flow inlets from three to nine enhances the fluid density and velocity, resulting in an increasing heat transfer coefficient and a decreasing Fanning friction factor.

- The increasing discharge rate increases the battery cell's internal resistance, which results in a high temperature. The maximum temperature at 1 C, 2 C, and 3 C are 31 °C, 34.6 °C, and 36.4 °C, respectively. Furthermore, the average heat transfer coefficient increases at high discharge rates due to the temperature approaching the pseudo-critical point and the friction factor slightly increasing due to density loss and velocity rise.

- The maximum temperature and temperature difference profiles decrease as the coolant mass flow rate increases. It is caused by an increase in turbulent intensity and a high Reynolds number of sCO_2, which strengthen the flow turbulence inside the cooling design. Also, the increasing mass flow rate achieved favorable heat transfer enhancement and acceptable pressure loss due to increased turbulence, which intensifies fluid mixing and further enhances the heat transfer between the fluid and the wall.

References

[1] O. Abedinia, M. Zareinejad, M. H. Doranehgard, G. Fathi, N. Ghadimi, Optimal offering and bidding strategies of renewable energy based large consumer using a novel hybrid robust-stochastic approach, Journal of Cleaner Production 215 (2019) 878–889.

[2] X. Deng, T. Lv, Power system planning with increasing variable renewable energy: A review of optimization models, Journal of Cleaner Production 246 (2020) 118962.

[3] M. Bartolozzi, Development of redox flow batteries. a historical bibliography, Journal of Power Sources 27 (3) (1989) 219–234.

[4] S. J. Kazempour, M. P. Moghaddam, M. Haghifam, G. Yousefi, Electric energy storage systems in a market-based economy: Comparison of emerging and traditional technologies, Renewable energy 34 (12) (2009) 2630–2639.

[5] I. Hadjipaschalis, A. Poullikkas, V. Efthimiou, Overview of current and future energy storage technologies for electric power applications, Renewable and sustainable energy reviews 13 (6-7) (2009) 1513–1522.

[6] X. Lai, Q. Chen, X. Tang, Y. Zhou, F. Gao, Y. Guo, R. Bhagat, Y. Zheng, Critical review of life cycle assessment of lithium-ion batteries for electric vehicles: A lifespan perspective, eTransportation (2022) 100169.

[7] Z. Chen, F. Xu, S. Cao, Z. Li, H. Yang, X. Ai, Y. Cao, High rate, long lifespan liv3o8 nanorods as a cathode material for lithium-ion batteries, Small 13 (18) (2017) 1603148.

[8] M. Fan, X. Chang, Q. Meng, L.-J. Wan, Y.-G. Guo, Progress in the sustainable recycling of spent lithium-ion batteries, SusMat 1 (2) (2021) 241–254.

[9] T. Zhang, L. Zhang, L. Zhao, X. Huang, W. Li, T. Li, T. Shen, S. Sun, Y. Hou, Free-standing, foldable v2o3/multichannel carbon nanofibers electrode for flexible li-ion batteries with ultralong lifespan, Small 16 (47) (2020) 2005302.

[10] Z. J. Baum, R. E. Bird, X. Yu, J. Ma, Lithium-ion battery recycling overview of techniques and trends (2022).

[11] Z. Siqi, L. Guangming, H. Wenzhi, H. Juwen, Z. Haochen, Recovery methods and regulation status of waste lithium-ion batteries in china: A mini review, Waste Management & Research 37 (11) (2019) 1142–1152.

[12] Y. Qi, F. Meng, X. Yi, J. Shu, M. Chen, Z. Sun, S. Sun, F.-R. Xiu, A novel and efficient ammonia leaching method for recycling waste lithium ion batteries, Journal of Cleaner Production 251 (2020) 119665.

[13] E. S. G. Challenge, Energy storage market report, US Department of Energy: December (2020).

[14] P. R. Hornsdale, Hornsdale power reserve in southern australia, Southern Australia: Septemeber (2017).

[15] J. B. Goodenough, Y. Kim, Challenges for rechargeable li batteries, Chemistry of materials 22 (3) (2010) 587–603.

[16] Y. Ji, Y. Zhang, C.-Y. Wang, Li-ion cell operation at low temperatures, Journal of The Electrochemical Society 160 (4) (2013) A636.

[17] S. Chacko, Y. M. Chung, Thermal modelling of li-ion polymer battery for electric vehicle drive cycles, Journal of Power Sources 213 (2012) 296–303.

[18] H. Park, A design of air flow configuration for cooling lithium ion battery in hybrid electric vehicles, Journal of power sources 239 (2013) 30–36.

[19] X. Han, L. Lu, Y. Zheng, X. Feng, Z. Li, J. Li, M. Ouyang, A review on the key issues of the lithium ion battery degradation among the whole life cycle, ETransportation 1 (2019) 100005.

[20] A. A. Pesaran, Battery thermal management in ev and hevs: issues and solutions, Battery Man 43 (5) (2001) 34–49.

[21] Z. Wang, Y. Wang, Z. Xie, H. Li, W. Peng, Parametric investigation on the performance of a direct evaporation cooling battery thermal management system, International Journal of Heat and Mass Transfer 189 (2022) 122685.

[22] W. Wu, S. Wang, W. Wu, K. Chen, S. Hong, Y. Lai, A critical review of battery thermal performance and liquid based battery thermal management, Energy conversion and management 182 (2019) 262–281.

[23] L. H. Saw, Y. Ye, A. A. Tay, Integration issues of lithium-ion battery into electric vehicles battery pack, Journal of Cleaner Production 113 (2016) 1032–1045.

[24] Q. Wang, B. Jiang, Q. Xue, H. Sun, B. Li, H. Zou, Y. Yan, Experimental investigation on ev battery cooling and heating by heat pipes, Applied Thermal Engineering 88 (2015) 54–60.

[25] M. B. Effat, C. Wu, F. Ciucci, Modeling efforts in the key areas of thermal management and safety of lithium ion battery cells: a mini review, Asia-Pacific Journal of Chemical Engineering 11 (3) (2016) 399–406.

[26] Z. Rao, S. Wang, A review of power battery thermal energy management, Renewable and Sustainable Energy Reviews 15 (9) (2011) 4554–4571.

[27] S. A. Khan, C. Eze, K. Dong, A. R. Shahid, M. S. Patil, S. Ahmad, I. Hussain, J. Zhao, Design of a new optimized u-shaped lightweight liquid-cooled battery thermal management system for electric vehicles: A machine learning approach, International Communications in Heat and Mass Transfer 136 (2022) 106209.

[28] P. Qin, M. Liao, D. Zhang, Y. Liu, J. Sun, Q. Wang, Experimental and numerical study on a novel hybrid battery thermal management system integrated forced-air convection and phase change material, Energy Conversion and Management 195 (2019) 1371–1381.

[29] J. Luo, D. Zou, Y. Wang, S. Wang, L. Huang, Battery thermal management systems (btms) based on phase change material (pcm): A comprehensive review, Chemical Engineering Journal 430 (2022) 132741.

[30] J. Zhang, D. Shao, L. Jiang, G. Zhang, H. Wu, R. Day, W. Jiang, Advanced thermal management system driven by phase change materials for power lithium-ion batteries: A review, Renewable and Sustainable Energy Reviews 159 (2022) 112207.

[31] K. Chen, M. Song, W. Wei, S. Wang, Design of the structure of battery pack in parallel air-cooled battery thermal management system for cooling efficiency improvement, International Journal of Heat and Mass Transfer 132 (2019) 309–321.

[32] D. S. Jang, S. Yun, S. H. Hong, W. Cho, Y. Kim, Performance characteristics of a novel heat pipe-assisted liquid cooling system for the thermal management of lithium-ion batteries, Energy Conversion and Management 251 (2022) 115001.

[33] J. Jung, Y. Jeon, H. Lee, Y. Kim, Numerical study of the effects of injection-port design on the heating performance of an r134a heat pump with vapor injection used in electric vehicles, Applied Thermal Engineering 127 (2017) 800–811.

[34] R. Van Gils, D. Danilov, P. Notten, M. Speetjens, H. Nijmeijer, Battery thermal management by boiling heat-transfer, Energy Conversion and Management 79 (2014) 9–17.

[35] M. S. Patil, J. Seo, Y. Bang, D. Kim, G. Ekanayake, G. Singh, H. Kim, Y. Choi, M. Lee, A novel design for lithium ion battery cooling using mineral oil, in: Proceedings of the 3rd International Mega-Conference on Green and Smart Technology (GST 2016), Jeju National University, Jeju island, Korea, 2016, pp. 21–23.

[36] J.-H. Seo, M. S. Patil, D.-W. Kim, Y.-M. Bang, M.-Y. Lee, Numerical study on the cooling performances of various cooling methods for laminated type battery, in: Proceedings of the 1st ACTS—Asian Conference on Thermal Sciences, 2017.

[37] M. S. Patil, J.-H. Seo, M.-Y. Lee, A novel dielectric fluid immersion cooling technology for li-ion battery thermal management, Energy Conversion and Management 229 (2021) 113715.

[38] K. Jithin, P. Rajesh, Numerical analysis of single-phase liquid immersion cooling for lithium-ion battery thermal management using different dielectric fluids, International Journal of Heat and Mass Transfer 188 (2022) 122608.

[39] J. Wei, Supercritical dielectric fluids for high power density applications, Ph.D. thesis, Georgia Institute of Technology (2021).

[40] R. Zalosh, P. Gandhi, A. Barowy, Lithium-ion energy storage battery explosion incidents, Journal of Loss Prevention in the Process Industries 72 (2021) 104560.

[41] E. W. Lemmon, M. L. Huber, M. O. McLinden, et al., Nist standard reference database 23, Reference fluid thermodynamic and transport properties (REFPROP), version 9 (2010).

[42] J. Xie, Z. Ge, M. Zang, S. Wang, Structural optimization of lithium-ion battery pack with forced air cooling system, Applied Thermal Engineering 126 (2017) 583–593.

[43] W. Nusselt, Das grundgesetz des wärmeüberganges, 1915.

[44] P. Guo, S. Liu, J. Yan, J. Wang, Q. Zhang, Experimental study on heat transfer of supercritical co2 flowing in a mini tube under heating conditions, International Journal of Heat and Mass Transfer 153 (2020) 119623.

[45] L. F. Cabeza, A. de Gracia, A. I. Fernández, M. M. Farid, Supercritical co2 as heat transfer fluid: A review, Applied thermal engineering 125 (2017) 799–810.

[46] M. S. Patil, S. Panchal, N. Kim, M.-Y. Lee, Cooling performance characteristics of 20 ah lithium-ion pouch cell with cold plates along both surfaces, Energies 11 (10) (2018) 2550.